A dual passive cavitation detector for localized detection of lithotripsy-induced cavitation *in vitro*

Robin O. Cleveland
Department of Aerospace and Mechanical Engineering, Boston University, Boston, Massachusetts 02215

Oleg A. Sapozhnikov
Department of Acoustics, Physics Faculty, M. V. Lomonosov Moscow State University, Moscow 119899, Russia

Michael R. Bailey and Lawrence A. Crum
Applied Physics Laboratory, University of Washington, Seattle, Washington 98105

(Received 18 June 1999; revised 10 August 1999; accepted 29 November 1999)

A passive cavitation detector (PCD) identifies cavitation events by sensing acoustic emissions generated by the collapse of bubbles. In this work, a dual passive cavitation detector (dual PCD), consisting of a pair of orthogonal confocal receivers, is described for use in shock wave lithotripsy. Cavitation events are detected by both receivers and can be localized to within 5 mm by the nature of the small intersecting volume of the focal areas of the two receivers in association with a coincidence detection algorithm. A calibration technique, based on the impulse response of the transducer, was employed to estimate radiated pressures at collapse near the bubble. Results are presented for the *in vitro* cavitation fields of both a clinical and a research electrohydraulic lithotripter. The measured lifetime of the primary growth-and-collapse of the cavitation bubbles increased from 180 to 420 μs as the power setting was increased from 12 to 24 kV. The measured lifetime compared well with calculations based on the Gilmore–Akulichev formulation for bubble dynamics. The radiated acoustic pressure 10 mm from the collapsing cavitation bubble was measured to vary from 4 to 16 MPa with increasing power setting; although the trends agreed with calculations, the predicted values were four times larger than measured values. The axial length of the cavitation field correlated well with the 6-dB region of the acoustic field. However, the width of the cavitation field (10 mm) was significantly narrower than the acoustic field (25 mm) as bubbles appeared to be drawn to the acoustic axis during the collapse. The dual PCD also detected signals from ''rebounds,'' secondary and tertiary growth-and-collapse cycles. The measured rebound time did not agree with calculations from the single-bubble model. The rebounds could be fitted to a Rayleigh collapse model by considering the entire bubble cloud as an effective single bubble. The results from the dual PCD agreed well with images from high-speed photography. The results indicate that single-bubble theory is sufficient to model lithotripsy cavitation dynamics up to time of the main collapse, but that upon collapse bubble cloud dynamics becomes important. [S0001-4966(00)02503-0]

PACS numbers: 43.80.Sh, 43.25.Yw, 43.35.Ei [FD]

INTRODUCTION

Shock wave lithotripsy (SWL) (Chaussy *et al.*, 1980) is the most common modality for treating kidney stones (Holmes and Whitfield, 1991). Despite the widespread use of SWL, there is no agreement in the literature as to the mechanism by which the shock wave destroys kidney stones. In addition, although early reports indicated that SWL treatment did not lead to appreciable damage to the kidney (Chaussy, 1982; Evan and McAteer, 1996), it is now recognized that a clinical dose of shock waves will induce renal injury in a majority, if not all, treated kidneys (Kaude *et al.*, 1985; Evan and McAteer, 1996). Both the significance of tissue damage, and the mechanisms that are responsible for the damage, are under dispute. There is an incentive therefore to develop techniques that can quantify the action of possible mechanisms in SWL.

One mechanism that appears to play a significant role during SWL, both for stone comminution and tissue damage, is acoustic cavitation. Acoustic cavitation refers to the growth and violent collapse of vapor or gas cavities in response to an acoustic pressure field. Cavitation has been proposed as a mechanism of stone comminution in SWL (Coleman *et al.*, 1987; Crum, 1988; Vogel and Lauterborn, 1988). Studies have shown that the presence of cavitation is critical to stone fragmentation *in vitro* (Sass *et al.*, 1991; Delacretaz *et al.*, 1995). Studies with biological systems demonstrate that significant bioeffects occur when cavitation is present (Delius *et al.*, 1990; Dalecki *et al.*, 1996). Evidence of cavitation events occurring in and around the kidneys of human patients during SWL has been detected (Coleman *et al.*, 1996). These results provide circumstantial evidence that in clinical lithotripsy cavitation could play both a beneficial role in stone destruction and a deleterious role in bioeffects. In this report a refinement of previous cavitation detection systems is presented which can both improve the spatial

specificity and better quantify the strength of cavitation events produced by a lithotripter.

At the focus of an electrohydraulic lithotripter, the pressure waveform consists of a shocked positive pulse, with peak pressure of order 40 MPa and duration 1 μs, followed by a negative tail, of about -10 MPa peak pressure and 4-μs duration (Coleman and Saunders, 1989). The behavior of cavitation bubble dynamics in response to a lithotripsy pressure pulse was predicted by Church (1989) based on the Gilmore–Akulichev model. The model predicts that bubbles will respond with a characteristic ''double-burst'' acoustic signature (discussed in more detail below). Coleman *et al.* (1992) measured the double-burst acoustic signature from cavitation in a lithotripter using passive cavitation detection (PCD). The PCD system consisted of a single focused hydrophone listening for acoustic emissions from the focal region of the lithotripter. The results showed that the measured response was qualitatively in accordance with the Gilmore–Akulichev model. Delacretaz *et al.* (1995) measured a double-burst signature from the cavitation field of an electromagnetic lithotripter using a polyvinylidene fluoride PVDF needle hydrophone. The double burst has also been recorded in patients undergoing clinical SWL (Coleman *et al.*, 1996). Measurements *in vivo* with a pig model indicated that tissue has a constraining effect on bubble dynamics (Zhong *et al.*, 1997, 1998, 1999).

A number of other techniques have been used to monitor lithotripsy-induced cavitation. When foil targets are placed in the focus of a lithotripter they suffer surface pitting due to cavitation. The pitting has been used to measure both the spatial extent and relative intensity of the cavitation (Coleman *et al.*, 1987; Lifshitz *et al.*, 1997; Bailey *et al.*, 1999) but does not give information on the time history of the bubble cloud. Pye and Dineley (1999) have recently published a technique where translation of a small sphere is used to detect cavitation. Sonoluminescence, light emissions from cavitation collapses, has been measured in the focal region of an electrohydraulic lithotripter (Coleman *et al.*, 1992). Laser scattering (Jochle *et al.*, 1996; Huber *et al.*, 1999) and fiber optic transmittance (Delacretaz *et al.*, 1995) provide time history of the bubble dynamics.

Perhaps the best measurements of the *in vitro* cavitation field are provided by high-speed photography (Sass *et al.*, 1991; Huber *et al.*, 1994; Jochle *et al.*, 1996; Zhong *et al.*, 1997, 1999). Video images demonstrate that cavitation in the free field consists of a large cloud of bubbles. This is significant for PCD systems because even with focused hydrophones it appears that detected emissions could come from a number of cavitation events. Difficulty in specifying the location of cavitation events using PCD is compounded in electrohydraulic lithotripters where spark jitter leads to variation in the location of the acoustic and hence the cavitation fields.

An advantage of the PCD over other methods is the ability to observe cavitation *in vivo*. This work describes an acoustic cavitation detection system, the dual PCD, which provides improved spatial information on the location of cavitation events in comparison to a single transducer PCD. The article first addresses the drawbacks associated with using a single focused transducer as a PCD. It proceeds to describe how signals from two focused PCD transducers, in association with a coincidence detection algorithm, can provide improved spatial localization of cavitation events. The dual PCD system is completed by establishing a calibration technique to estimate the pressure radiated by collapsing cavitation bubbles. The dual PCD was used to map the cavitation field of two electrohydraulic lithotripters and results were compared to numerical predictions of single-bubble dynamics. The presence of bubble rebounds detected by the dual PCD was confirmed with high-speed photography. The dual PCD system described here has the potential to detect events *in vivo* and may be a useful tool in elucidating the role of cavitation in clinical lithotripsy by providing a means to correlate cavitation with either stone fragmentation or tissue injury.

I. MATERIALS AND METHODS

A. Lithotripters

The majority of the measurements were conducted in the research electrohydraulic lithotripter at the Applied Physics Laboratory, University of Washington at Seattle (APL-UW), which was designed to mimic the performance of a clinical lithotripter, the Dornier HM3 (Howard and Sturtevant, 1997; Cleveland *et al.*, 2000). Measurements were also taken on a clinical, unmodified, Dornier HM3 lithotripter at Methodist Hospital (Indianapolis, Indiana). Our experiments are focused on the Dornier HM3 because it is the lithotripter in the widest use in the United States (Lingeman, 1996). The acoustic field of the lithotripters was characterized by a broadband polyvinylidene fluoride (PVDF) membrane hydrophone with a 0.5-mm active spot (Model 702, Sonic Industries, Hatboro, Pennsylvania). The calibration value provided with the shock wave hydrophone was confirmed by substitution calibration, up to 20 MHz, with a PVDF membrane hydrophone (type Y-33-7611, GEC-Marconi, Chelmsford, UK) that had been calibrated at National Physical Laboratories (Teddington, UK). The waveforms and acoustic fields measured in the two lithotripters have been determined to be similar (Cleveland *et al.*, 2000). In each lithotripter, peak positive pressure was variable from 25 MPa (12 kV) to 40 MPa (24 kV).

An electrohydraulic lithotripter uses an underwater spark to generate a shock wave. The spark is located at the internal focus ($F1$) of a hemi-ellipsoidal reflector; the reflector focuses the spherical shock wave generated by the spark to the external focus ($F2$) of the ellipsoid. The geometry of the ellipses in the two lithotripters was identical (major half-axis $a=139$ mm, minor half-axis $b=78$ mm; the reflector is truncated to be 14 mm short of complete hemi-ellipsoid). Both lithotripters used an 80-nF capacitor to store the high voltage before discharging it through a refurbished Dornier electrode (Service Trends, Kennesaw, Georgia). Electrodes with between 100 and 2000 sparks were used to limit variability in spark amplitude with electrode age. The water in both lithotripters was degassed to between 2 to 4 ppm of O_2 (approximately half the gas content of tap water) and NaCl added to achieve a conductivity of 650 μS/cm. Gas content

was measured to increase during experiments at a rate of 0.1 ppm/hour. The temperature of the water bath in the APL-UW machine was 20 °C; the HM3 water was maintained at body temperature 37 °C. In the HM3, positioning was achieved using the three-axis hydraulic positioner provided with the HM3, or by the mounting hand-controlled stages on the side of the tank. Positioning in the APL-UW lithotripter was accomplished using a computer-controlled three-axis system (Velmex-Unislide, Bloomfield, NY).

All data were recorded on a digital oscilloscope (Tektronix TDS 744, Beaverton, OR) which has an 8-bit digitizer and sampling rate up to 2 gigasamples/s. The scope was triggered by a photodiode which detected the light flash from the underwater spark discharge. Data were transferred to computer and processed by LabVIEW (National Instruments, Austin, TX). Further processing was done in MatLab (Mathworks, Natick, MA).

B. Bubble dynamics model

Measurements of cavitation activity were compared with results of numerical calculations. The model used for bubble dynamics was the Gilmore–Akulichev formulation (Gilmore, 1952; Akulichev, 1971), with gas diffusion included. The model was proposed and solved numerically for lithotripsy by Church (1989). We have reproduced Church's numerical solution and briefly review the model here; further details can be found elsewhere (Church, 1989; Chol *et al.*, 1993). The Gilmore equation describes the oscillations of a single spherical bubble driven by an acoustic excitation and can be written in the following form:

$$\left(1-\frac{\dot{R}}{c}\right)R\ddot{R}+\frac{3}{2}\left(1-\frac{\dot{R}}{3c}\right)\dot{R}^2=\left(1+\frac{\dot{R}}{c}\right)H+\frac{R}{c}\left(1-\frac{\dot{R}}{c}\right)\frac{dH}{dt}, \tag{1}$$

where R is the bubble radius, a dot indicates a time derivative, t is time, c is the speed of sound in the liquid at the bubble wall, and H is the difference in the liquid enthalpy between the bubble wall and infinity. The expressions for $c=\sqrt{dp/d\rho}$ and $H=\int_{p_\infty}^{p(R)}dp/\rho$ were obtained from the Tait equation of state for the liquid $p=p_0+(c_0^2\rho_0/n)\cdot[(\rho/\rho_0)^n-1]$, where n is the Tait parameter, p_0 is ambient pressure, ρ_0 ambient density, and c_0 small-signal sound speed. The upper limit of the enthalpy integral is the pressure at the water–gas interface, i.e., the bubble wall $p(R)=p_g-2\sigma/R-(4\mu/R)\dot{R}$, where p_g is the pressure in the gas, given below, σ is the coefficient of surface tension, and μ the coefficient of viscosity. The lower limit is $p_\infty=p_0+P(t)$, the pressure at infinity where $P(t)$ is acoustic pressure associated with the lithotripter shock wave.

Gas diffusion was accounted for by Church with a zero-order model for gas diffusion based on a theory by Eller and Flynn (1965). The number of moles of gas $n(t)$ in the bubble is given by the following equation: $n=n_0-4\sqrt{\pi D}\int_0^\tau F(\tau')\times(\tau-\tau')^{-1/2}d\tau'$, where n_0 is the initial number of moles in the bubble, D is the diffusion constant, $\tau=\int_0^t R^4(t')dt'$, $F(\tau)=C_0(p_g/p_0)-C_i$, C_0 the saturation concentration of the gas in the liquid, C_i the initial concentration of gas in the liquid far from the bubble, $p_g=(p_0+2\sigma/R_0)(n/n_0)\times(R_0/R)^{3\eta}(R_{0n}/R_0)^{3(\eta-1)}$ is the pressure in the gas, R_0 the initial radius, R_{0n} the time varying equilibrium radius, and η is the polytropic exponent of the gas.

The radiated pressure was calculated using the Akulichev formulation

$$p_{\mathrm{RAD}}(t)=p_0+\frac{\rho_0 c_0^2}{n}\left[\left(\frac{2}{n+1}+\frac{n-1}{n+1}\times\sqrt{1+\frac{n+1}{rc_0^2}G}\right)^{2n/(n-1)}-1\right], \tag{2}$$

where $G=R(H+U^2/2)$ is an invariant of the bubble motion evaluated at the bubble wall and r is the distance from the center of the bubble. Equation (2) does not account for nonlinear distortion of the radiated pressure as it propagates from the bubble.

The equations were solved using a code written in FORTRAN. The Gilmore equation was integrated using the fourth-order Runge–Kutta solver from Numerical Recipes (Press *et al.*, 1992, pp. 710–722). The diffusion equation was solved using a trapezoidal rule as discussed by Church (1989). The various numerical values used for the parameters were $p_0=10^5$ Pa, $c_0=1485$ m/s, $\rho_0=1000$ kg/m^3, $n=7$, $\sigma=0.0725$ N/m, $\mu=0.001$ Pa.s, $n_0=6.93\times10^{-15}$ moles, $D=2.42\times10^{-9}$ m^2/s, $C_0=0.872$ moles/m^3, $C_1=0.436$ moles/m^3 (i.e., 50% gas saturation), $\eta=1.4$, and $R_0=3$ μm. The acoustic pressure $P(t)$ used as an input to the code was taken from waveforms measured by the shock wave hydrophone system (Sec. I A). The waveforms were sampled at 250 MHz (4 ns) and linear interpolation was used to produce a continuous waveform.

Figure 1 shows a sample calculation of a bubble in response to an acoustic waveform measured in the APL-UW lithotripter. Figure 1(a) shows the measured pressure waveform and a corrected waveform. The corrected waveform has an elongated negative pressure tail (Bailey *et al.*, 1999) to compensate for an underestimation of the negative pressure phase attributed to measurements with PVDF membranes (Wurster *et al.*, 1994). In all the bubble dynamics calculations presented here, corrected pressure waveforms were used for the acoustic input. Figure 1(b) and (c) show the radius of the bubble and the radiated pressure 10 mm away from the bubble as functions of time. The response of a bubble consists of an initial collapse due to the positive-pressure phase of the shock and the corresponding first burst acoustic emission p_S^* (the asterisk indicates a computed value). This is followed by a rapid growth phase driven by the negative-pressure tail of the shock wave. The inertia imparted to the bubble wall by the negative tail is large enough that the bubble continues to grow after the shock wave has passed. From this point inertial cavitation dominates, as there is no external time-varying driving pressure, and the bubble continues to grow for a relatively long period (in excess of 100 μs). Eventually the ambient pressure in the fluid stops the growth and initiates an inward flow of fluid which leads to a second collapse of the bubble and the corresponding second burst of the acoustic emission, p_C^*. These two emissions are the double-burst signature and the time between them is the characteristic time t_C^*. After the second collapse

the bubble undergoes a number of growth and collapse cycles, rebounds, at the collapse of each rebound a pressure wave is radiated $p_R^*, p_{R2}^*, \ldots$ and the time between rebounds is $t_R^*, t_{R2}^*, \ldots$ When the bubble becomes quiescent we note that its radius has increased to approximately 60 μm because of gas diffusion into the bubble.

For the simulation shown in Fig. 1 the characteristic time was about 520 μs, the maximum radius 3 mm, and the rebound time 33 μs. At distance 1 cm from the bubble center the calculated radiated pressures were: $p_S^* = 0.8$, $p_C^* = 68$, and $p_R^* = 0.24$ MPa. These values are similar to those calculated by Church. We note that the radiated pressure expression does not account for nonlinear distortion of the radiated pressure wave. For the pressures predicted, particularly at the second collapse, the radiated pressure wave will form a shock within 10 mm and suffer corresponding nonlinear attenuation which will reduce the collapse pressures p_C^*. Neglect of nonlinear distortion may contribute to calculated radiated pressures being larger than measured values.

C. Cavitation detection receivers

The system for measuring cavitation signals is now presented. Although the dual PCD system consists of two focused receivers, we first discuss the behavior of a single PCD receiver. The individual transducers used in this research were spherical caps of C-5400 lead zirconate titanium (PZT) (Channel Industries, Santa Barbara, CA) with a resonance frequency of 1.08 MHz, aperture diameter of 100 mm, and radius of curvature (focal length) of either 100 or 200 mm. The PZT elements were mounted in a stainless steel housing and were air-backed. When used as receivers of acoustic emissions from shock waves it was necessary to use a high-pass filter (model 3202, Krohn-hite, Avon, MA), with a 300-kHz cutoff frequency, to remove the low-frequency signal of the radial mode of the transducer (approximately 20 kHz). The configuration used here is very similar to that described by Coleman *et al.* (1992).

The use of focused transducers in PCD is based on the desire to detect cavitation events from a confined volume. Although focused transducers have a narrow focal region, the focal region can be relatively long, leading to uncertainty in the axial location of a detected event. The size of the sensitive region of a focused hydrophone can be determined from the radiation pattern of the transducer. Because of reciprocity of the wave equation, the focal region of the transducer as a hydrophone is identical to the focal region of the transducer as a source. The acoustic field of a focused piston source was described theoretically by O'Neil (1949), and it has been shown that a focused piezoelectric transducer behaves very much like an ideal focused piston source (Cathignol *et al.*, 1997). The O'Neil solution for pressure amplitude distribution along the transducer axis for sinusoidal excitation can be written as

$$p = V_0 \rho c \left| \frac{e^{i2\pi z/\lambda} - e^{i2\pi R/\lambda}}{1 - z/F} \right|, \tag{3}$$

where V_0 is the amplitude of the normal velocity of the piston surface, ρ the ambient density of the medium, c the small signal sound speed, z the distance along the axis, λ the wavelength, F the radius of curvature, and R the distance from the observation point to the transducer edge. The axial pressure field described by Eq. (3) achieves a localized region of high amplitude around the geometrical focus $z = F$. The axial length of the ''focal spot'' $\Delta_\parallel$ (full width half-maximum) is given by

$$\Delta_\parallel = \frac{0.6\lambda}{\sin^2(\alpha/2)}, \tag{4}$$

where $\alpha = \arcsin(a/F)$ is the half-aperture angle of the radiator, and a the radius of the transducer. The lateral distribution of the pressure amplitude at the focal plane ($z = F$) may be expressed as follows:

$$p = p_{\max} \left| \frac{2J_1(2\pi r \sin\alpha/\lambda)}{2\pi r \sin\alpha/\lambda} \right|. \tag{5}$$

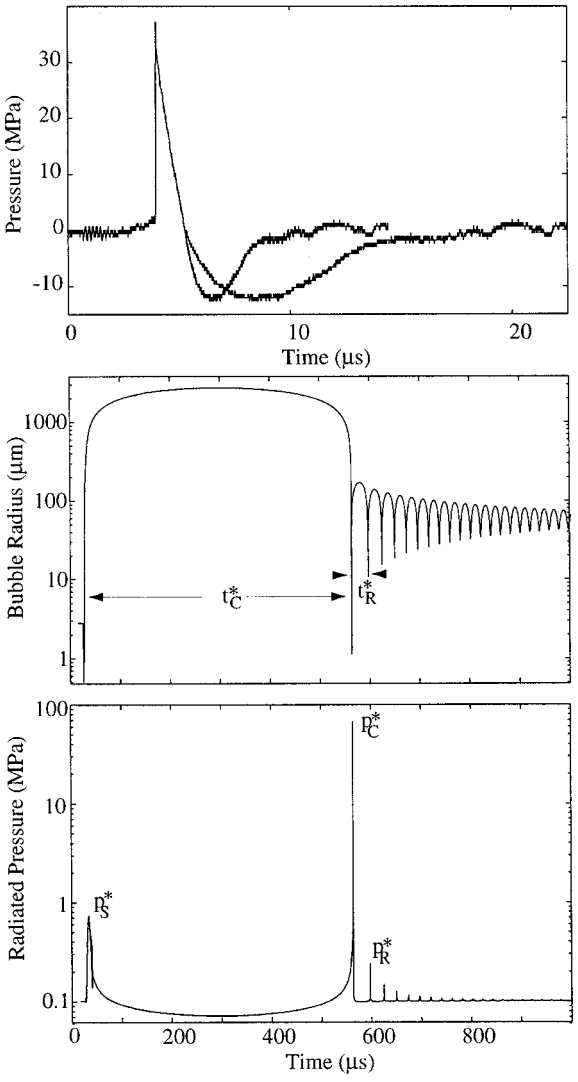

FIG. 1. Predicted bubble dynamics in the APL-UW lithotripter at 24 kV (a) measured acoustic shock wave and corrected shock wave used for bubble dynamics, (b) calculated radius time curve of a 3-μm bubble, (c) calculated radiated pressure 10 mm from the bubble. The scattered pressure p_S*, characteristic time t_C*, radiated collapse pressure p_C*, rebound time t_R*, and radiated rebound pressure p_R* are all indicated. The asterisk * denotes the values are calculated.

TABLE I. Axial and lateral dimensions of sensitive volume for different PCD transducers: 1, 2, Channel Industries, 3 Coleman *et al.* (1992, 1996), 4 Zhong *et al.* (1997).

Hydrophone #	1	2	3	4
f_{res}, MHz	1.08	1.08	1.0	1.0
$2a$ (mm)	100	100	100	38
F (mm)	100	200	120	102
$\Delta_{\parallel}$, mm	13	53	20	105
$\Delta_{\perp}$, mm	2.0	3.9	2.5	5.7

Here p_{max} is the pressure amplitude at the focal point, J_1 the cylindrical Bessel function of the first order, and r the lateral distance. The full width half-maximum diameter of the focal region is

$$\Delta_{\perp} = \frac{0.7\lambda}{\sin\alpha}. \tag{6}$$

Equations (4) and (6) define the axial and lateral dimensions of the sensitive area of a single PCD transducer. When sensing cavitation events from the bubble cloud, a single PCD transducer receives signals coming from all collapsing bubbles sitting in a cigar-shaped volume of dimensions $\Delta_{\parallel}$ by $\Delta_{\perp}$.

Table I presents corresponding values for the PCD transducers we employed (Nos. 1 and 2), the PCD transducer used by Coleman *et al.* (1992, 1996) (No. 3), and the PCD transducer used by Zhong *et al.* (1997) (No. 4). Table I illustrates that all PCD transducers have good spatial resolution, of the order of a few millimeters, in the lateral direction ($\Delta_{\perp}$), but have a poor resolution, of the order of tens of millimeters, in the axial direction ($\Delta_{\parallel}$). The resolution is especially poor for small aperture (i.e., small α) PCD transducers, which can be deduced from the $\sin\alpha$ term in the denominator of both Eqs. (4) and (6).

D. Coincidence detection: dual PCD

Dual PCD, illustrated in Fig. 2, uses two perpendicular confocal transducers to produce a detector with an effective focal dimension proportional to the width, not the length, of the focal region of each transducer. Although each receiver in the dual PCD suffers from the same long focal region as a single PCD, it is possible to take advantage of the fact that signals coming from the union of the two focal regions will have the same arrival time. A coincidence detection algorithm was constructed so that only events that originated from the effective focal region were identified as cavitation events. The transducers were mounted on a rigid frame but each transducer could be independently rotated and moved vertically. Fine alignment was achieved by placing a needle hydrophone at the desired focus; each of the PCD transducers was used as a source and independently positioned so that a maximum signal was recorded at the needle.

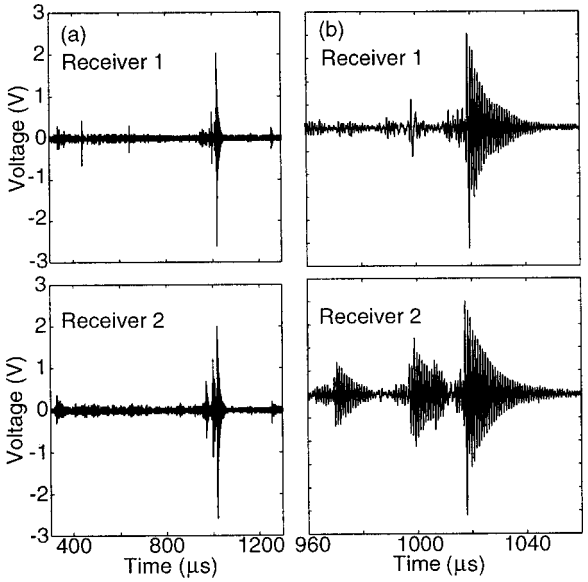

FIG. 3. Dual PCD signals for a single shock wave at 24 kV (a) long time scale, (b) closeup of main burst.

The concept behind the use of coincident detection using the dual PCD is illustrated by an example. Figure 3 presents signals registered by the two confocal PCD transducers (200-mm focal length) aligned with the focal region of the APL-UW lithotripter for a single spark discharge at a voltage of 24 kV. Figure 3(a) shows the signals received by both transducers, where zero time corresponds to the firing of the spark. The travel distance of the shock wave from the electrode to the reflector, and then to $F2$ is 276 mm; the distance from $F2$ to either PCD hydrophone is 200 mm. The time delay for the total distance is 317 μs, assuming a speed of sound 1500 m/s, which corresponds to the first peak seen in Fig. 3(a). This first signal p_S results from nonlinear acoustic scattering, which can be interpreted as being comprised of two inseparable effects: (i) scattering of the lithotripter shock wave from small bubbles or particles that are typically present in water; (ii) acoustic radiation from the bubbles during their first collapse. As described in Sec. I B, the cavitation field then proceeds through a growth and collapse cycle and radiates a second acoustic emission p_C. In Fig. 3 a sec-

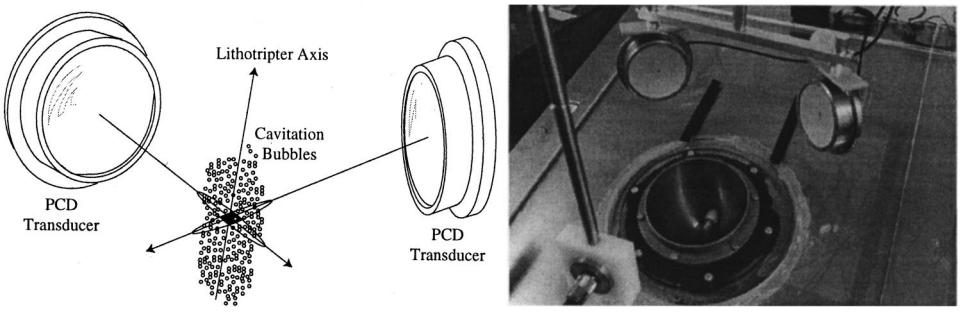

FIG. 2. Diagram of the concept of intersecting focal volumes is shown on the left. The cigar-shaped volumes are the focal regions of the individual transducers; the shaded region is the effective focal volume of the dual PCD. On the right is a photograph of the dual PCD in APL lithotripter. The brass ellipsoidal reflector and spark plug are at the bottom of the tank; the two confocal bowls are also confocal with $F2$ of the ellipsoid.

ond, large amplitude, emission is detected by both PCD transducers at around 1000 μs; however, additional emissions are registered by both transducers before and after this event. Figure 3(b) shows a closeup view of the signal around 1000 μs which consists of a number of ''events.'' Each event consists of a decaying sinusoid, the impulse response of the transducer. The signal from one PCD transducer does not allow one to deduce whether the detected events originated in the focal region or not. The structure of the detected signals becomes clear when comparing signals from the two PCD transducers. Only the signals arriving at similar times and having similar amplitude are of interest, all other signals do not originate near the effective focal region of the dual PCD. It is apparent from the traces that only the burst arriving at 1017 μs is similar on both transducers, therefore only this burst corresponds to a bubble collapsing in the effective focal region. The characteristic time in this case is $t_C = 700\,\mu$s.

Note that, in addition to the main collapse, a further simultaneous collapse, at approximately 1260 μs, is also apparent from the dual PCD traces. This second collapse appears to be from a ''rebound,'' a second growth-and-collapse cycle, and occurs about 240 μs after the main collapse. The rebound will be discussed in more detail in Sec. II.

The signals displayed in Fig. 3 were unwieldy to perform analysis on. Significant data reduction was achieved by demodulating the signals to remove the sinusoidal oscillations yet maintain the structure of the envelope. The demodulation process was carried out in LABVIEW immediately after the waveforms had been transferred from the digital oscilloscope to the computer. A full-wave rectification demodulation process was used; it consisted of taking the absolute value of the signal, followed by a low-pass filter (Butterworth, 300 kHz, second order) and finally decimation by a factor of five. The demodulation process also reduced the peak amplitude of the signal by a factor of 2.5.

Detection of simultaneous events was carried out in post-processing using MatLab by the following procedure. The demodulated signals from each channel were converted from volts to pressure by a calibration factor (described in the following section). The first burst (corresponding to the arrival of the shock) was located by windowing each waveform to within 20 μs of the calculated arrival time of the first burst. The windowed waveforms were oversampled by a factor of five to smooth the signals and then the peak in the cross correlation between the two channels was used to determine the location of the first burst. The second burst, associated with the primary inertial collapse, was determined by finding the location of the maximum signal (for time greater than 20 μs after the first burst) on each channel. The 20-μs delay was used to skip over spurious signals associated with the coda of the first burst. For each of the maxima, the two channels were windowed from -10 to 30 μs around the time of the peak (large enough to capture the impulse response of the PCD), locally resampled and a cross correlation performed. If a maximum occurred in the cross correlation for time shifts less than 3.4 μs (which corresponded to the 5-mm cross-sectional region of the PCD transducers), a coincident event was deemed to have occurred. Rebounds were found by looking for maxima in the recorded signals beyond the primary collapse by performing the same windowing and cross-correlation algorithm.

Once coincident events were identified, the signal (or pulse) amplitudes on each channel were compared to determine if the event had occurred at the focus. Coincident events do not necessarily occur at the focus; because only two transducers were used coincident events could in fact occur anywhere in the equal travel-time plane that bisects the two transducers. However, the focused nature of the transducers meant that events outside of the focal region, but which still lie on the plane of equal travel time, were detected with very low amplitude. These events were identified and excluded on two grounds: (1) if the amplitude of the signals received on the two channels differed by more than a factor of three it was assumed that the bubble was outside of the focal region of one of the transducers and (2) if the amplitude of the signal from the second burst was less than twice the amplitude of the signal received from the first burst, i.e., $p_C < 2p_S$, it was assumed that the bubble was not in the focal region. The signal from the first burst was very consistent and it appeared that there was always some sort of bubble or scatterer present to generate this signal in the focal region of the dual PCD. For a cavitation event to occur in the first side lobe of a PCD and appear to have come from the focal zone (that is, exceed the detection threshold given here) would require a collapse pressure in excess of 30 MPa which was larger than anything we measured. In summary, a ''focal event'' was deemed to have occurred when

(1) The arrival times of the pulses on both channels were close enough for the event to have been somewhere on the plane of constant travel time for the transducers.
(2) The amplitudes of both pulses were consistent with a signal emanating from the focal region of both transducers.

The action of the algorithm is demonstrated in Fig. 4, which shows demodulated signals received by a pair of transducers (PCD#2, $F = 200$ mm) from five consecutive shots. The lithotripter was at a setting of 18 kV and fired approximately every 3 sec (limited by the time necessary to transfer data from the scope to the computer). For the signals in Fig. 4 the focus of the dual PCD was aligned 10 mm in front of $F2$ of the lithotripter. The signal from the second PCD transducer was inverted to assist in visual comparison of the signals. The vertical scale has been calibrated to represent the peak radiated pressure 10 mm from the bubble center as discussed below in Sec. I E.

Locations where a maximum in the cross correlation was detected (not necessarily a focal event) are marked by an ''$\times$.'' The uppermost traces (shot 1 of the five) show no significant emissions on either channel. Shot 2 shows cavitation activity on channel 1 only but no activity on channel 2. The third shot yielded a coincident event (simultaneous signals on both channels) but of such low amplitude that it was assumed the signals did not originate from the focal region of the dual PCD. Shot 4 shows an event and apparent rebound detected on channel 2 but no events on channel 1, which indicates the cavitation collapse was in the focal re-

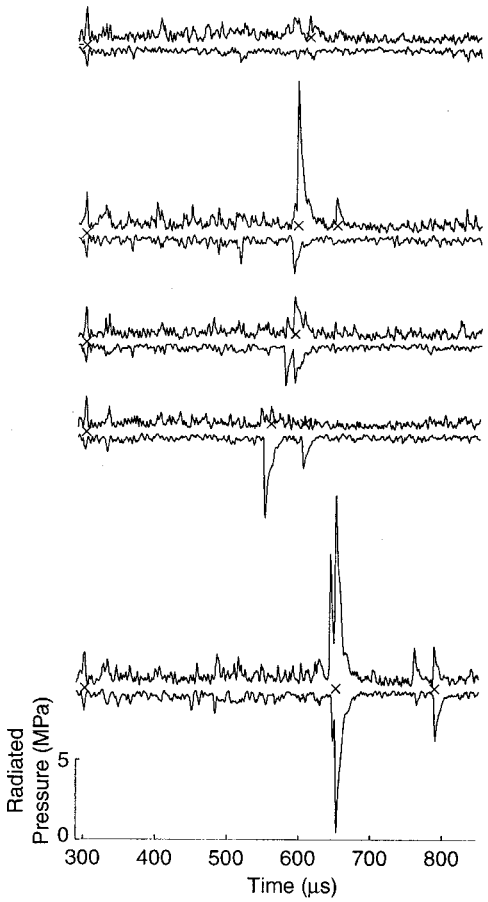

FIG. 4. Five consecutive dual PCD recordings at 18 kV. The radiated pressure is calibrated in terms of the peak pressure at a distance 10 mm from a collapsing bubble. The shape of the waveform is related to the impulse response of the PCD transducer and is not representative of the pressure waveform of the acoustic emission.

gion of transducer 2 but outside the focal region of transducer 1. The last shot shows a large cavitation event at 650 μs and a rebound signal at 800 μs evident on both channels—the algorithm described above identified this as a focal event. The collapse time, or characteristic time, $t_C = 340\,\mu$s, is the time between the first collapse $p_S = 2.2$ MPa and the main collapse $p_C = 12$ MPa. The rebound time t_R was 150 μs and the radiated pressure $p_R = 3.3$ MPa. Note that upon examination of the traces associated with the last shot there appeared to be a second bubble nearby that collapsed a little sooner than the bubble that was detected. This second bubble also appeared to generate a rebound. The coincident detection algorithm rejected this signal as being outside the volume of interest because the signal was disproportionately strong on channel 1.

Measurements taken at the focus of the lithotripters studied here provided simultaneous cavitation events for approximately 2/3 of the shots at 18 kV. Observation with a single PCD transducer would lead one to observe cavitation events in at least 90% of the shots because it does not exclude events outside of the focal region.

E. PCD pressure calibration

In addition to being able to localize cavitation events it was also considered useful to obtain an estimate of the amplitude of the acoustic emission generated by the cavitation collapse. Calculations by Church (1989) predict that the second collapse produces an outgoing shock wave with peak pressure of order 30 MPa at a distance of 1 cm from the bubble. Pressures nearer the bubble would be higher. Vogel and Lauterborn (1988) performed an experiment with a single laser-produced vapor bubble. They measured the amplitude of the pressure wave radiated by a collapsing bubble at a distance of 1 cm from its center. For the same maximum bubble radius as in the calculations of Church, their measurements give a value of about 10 MPa, which is three times less than corresponding computed value. Our goal was to estimate, from the PCD signals, the pressure generated by a bubble excited by a lithotripter pulse.

Calibration of a single PCD system has been reported by Zhong *et al.* (1997). The calibration value was the sensitivity of their transducer at resonance. Based on this technique they report that the pressure 10 mm from a cavitation bubble consisted of a pulse with 1.8 MPa compressive pressure and a 3.3-MPa tensile pressure for a spark discharge of 18 kV. These values are an order of magnitude less than predicted by Church, and in addition, it seems unlikely that a collapsing bubble will produce a stronger tensile pulse than compressive pulse. We discuss below that a resonance calibration is not appropriate for extracting the peak amplitude of pulse-type excitations.

The acoustic waveform detected by the PCD transducer cannot be easily reconstructed from the voltage it produces. The transducer is a high-Q resonator and its response to cavitation emission is a tone burst with exponentially decaying envelope, as seen in Fig. 3(b). Therefore the sensitivity of the transducer at its resonant frequency G_0 cannot be used for determining the pressure amplitude of a wide bandwidth signal such as the radiation from a bubble collapse. The measured voltage $u(t)$ from the PCD transducer can be described as a convolution of the incident acoustic pressure $p(t)$ and $h(t)$ the impulse response of the transducer,

$$u(t) = \int_{-\infty}^{\infty} h(t')p(t-t')dt'. \tag{7}$$

If $h(t)$ is known it is technically possible to recover the pressure waveform by deconvolving the impulse response from the measured signal. Unfortunately, if the pressure pulse is wideband and the receiver narrow band, as is the case here, then the presence of noise leads to significant errors in the inversion process (see, e.g., Press *et al.*, 1992, pp. 547–549).

We propose a new calibration scheme to estimate the amplitude of a pressure wave radiated during lithotripsy bubble collapse. For excitation by a very short pulse, as occurs in emissions from a bubble collapse, a simple approximation for the transducer response can be made which allows a calibration value to be determined from the impulse response of the transducer. If the incident wave is shorter than the resonant period of the transducer (about 1 μs for the PCD transducers used here), the excitation is effectively an impulse function to the PCD transducer and Eq. (7) reduces to

$$u(t) = h(t) \cdot \int_{-\infty}^{\infty} p(r,t')dt', \tag{8}$$

i.e., the PCD transducer responds with its impulse response scaled by a factor that depends on the integral of the acoustic pulse over time.

We determine whether the acoustic pulse from a cavitation bubble is short enough from measurements of Vogel and Lauterborn (1988). They reported that a shock wave emitted by a collapsing bubble has an exponential waveform,

$$p(t) = p_0 \cdot H(t) e^{-t/\tau_0}, \tag{9}$$

where $H(t)$ is the Heaviside step function.[1] Their measurements gave $\tau_0 = 35$ ns and $p_0 = 10$ MPa at 10 mm from the bubble center. We require that the duration of the pulse at the face of the PCD transducer (a distance of 100 mm from the bubble) be short compared to 1 μs. The pulse is intense enough that nonlinear distortion will occur as it propagates from the bubble to the PCD transducer; the distortion will lead to an increase of the duration of the pulse and decrease in amplitude (more rapidly than given by spherical spreading) (see, e.g., Rudenko and Soluyan, 1977, p. 36; Blackstock *et al.*, 1998, pp. 102–110). In the case of spherically spreading shock waves it is possible to use weak shock theory to model the nonlinear effects. For the waveform measured by Vogel and Lauterborn: $p_0 = 10$ MPa, $\tau_0 = 35$ ns, at $r_0 = 10$ mm, spherical spreading, without nonlinear effects, would predict that at $r = 100$ mm, $p = 1$ MPa, and $\tau = 35$ ns. When nonlinear effects are taken into account one calculates $p = 0.41$ MPa and $\tau = 130$ ns. Therefore, nonlinearity distorts the waveform, reducing the peak pressure more than two times and increasing the pulse duration almost four times. The duration is still much shorter than the period of oscillation of the hydrophone (926 ns at 1.08 MHz) and the approximation given in Eq. (8) is valid. A useful property of the nonlinear distortion that we shall also exploit is that the area under pressure curve is independent of nonlinear distortion, i.e., $S(r) = \int_{-\infty}^{\infty} p(r,t')dt'$ will vary according to linear theory (spherical spreading in this case) therefore $S(r) = S(r_0) r_0 / r$. For the Vogel and Lauterborn pulse the time integral at the source is $S(r_0) = p_0 \tau_0$.[2]

We now need to determine $h(t)$, the impulse response of the transducer for Eq. (8). This was done by placing a PZT needle hydrophone of 0.635-mm active element diameter (Dapco Industries, Ridgefield, CT) at the focus of the PCD transducer. The PZT needle had a 6-dB bandwidth that covered the frequency range 1 to 10 MHz. The needle was excited by a short, 0.5-μs duration, electrical pulse; the bandwidth of the needle was broad enough that it generated an acoustic pulse that was as short as the electrical signal. The short duration was confirmed by measuring the acoustic signal with the Marconi PVDF membrane mentioned above. The response of the PCD transducer to the acoustic impulse was similar to those in Fig. 3(b), and it appeared to be an exponentially damped sinusoid, which is typical for a simple damped resonance system. The measured waveform was assumed to be a good representation of the impulse response and was fitted to the following function:

$$h(t) = h_0 e^{-t/\tau^*} \sin 2\pi f_{\text{res}} t, \tag{10}$$

where the parameters h_0, τ^*, and f_{res} were to be determined. The resonant frequency f_{res} was determined from the period of oscillation of the impulse response. The decay constant τ^* was determined from the envelope of the impulse response.

Accurate determination of the parameter h_0 directly from the damped sinusoid was found to be difficult as it involved extrapolation of the exponential envelope. Instead h_0 was determined from the response at resonance G_0; for a sinusoidal excitation $p = p_{\max} \sin 2\pi f_{\text{res}} t$, the peak measured voltage $u_{\max} = G_0 p_{\max}$. Equations (7) and (10) predict that the peak measured voltage is also given by $u_{\max} \approx p_{\max} h_0 \tau^*/2$ and therefore $h_0 = 2G_0/\tau^*$. The sensitivity at resonance G_0 was determined by exciting the PZT needle with a 20-Vpp, 40-cycle tone burst at f_{res}. The 40-cycle pulse was long enough that the transducer attained steady state while avoiding reverberation problems in the tank. First, the field of the needle was measured with the Marconi hydrophone to confirm that it behaved as a spherical wave along the axis and to determine the acoustic pressure at the face of the transducer p_{face}. Then the PZT needle was placed at the focus of one of the PCD transducers and the peak voltage V_R from the transducer was recorded. If the PZT needle were an ideal spherical source the sensitivity of the bowl at resonance would be $G_0 = V_R / p_{\text{face}}$. However, a correction was necessary because the needle source was not perfectly omnidirectional. The PZT needle can be considered a piston source with a directivity function given by $D(\theta) = 2J_1(2\pi a \sin\theta/\lambda)/2\pi a \sin\theta/\lambda$, where a is the source radius, and θ the observation angle from the axis. We measured the transverse amplitude distribution of the PZT needle and it compared well with the Bessel directivity function. As the transducer response is a result of averaging of pressure over its surface, it is necessary to correct for the change in amplitude across the face of the transducer. This procedure gives a 3% correction to the sensitivity of the 100-mm focal length bowl and a 1% correction for the 200-mm focal length bowl, i.e., the effect of the directivity pattern of the PZT needle was very small. The resonant sensitivity for the 100-mm bowl was $G_0 = 111$ V/MPa. For the case of the pair of 200-mm bowls the resonant frequency sensitivities were $G_0 = 118$ and $G_0 = 164$ V/MPa.

Once the response of the transducers had been characterized it was possible to determine the calibration. The short duration of the excitation indicates that the response is given by Eq. (8); it follows from the form of the impulse response that the peak voltage from the transducer will be $u_{\max} = h_0 S(r)$. We noted above that for nonlinear distortion of the exponential pulse the pulse integral $S(r) = p_0 \tau_0 r_0 / r$, where p_0 is the peak pressure and τ_0 the shock wave duration at a distance r_0 from the bubble. It is now possible to determine the peak pressure of the radiated acoustic emission at a distance r_0 from the center of the collapsing bubble,

$$p_0 = u_{\max} \cdot \frac{r\tau^*}{2G_0 r_0 \tau_0}. \tag{11}$$

Here r is distance from the center of the bubble to the surface

of the PCD transducer, that is, the focal distance of the transducer.

For the case of the 100-mm bowl the appropriate values are $r=100\,\text{mm}$, $\tau^*=7.4\ \mu\text{s}$, and $G_0=111\,\text{V/MPa}$. The only value we did not measure was τ_0, which we took to be 35 ns from the measurements of Vogel and Lauterborn (1988). The calibration value relating the maximum voltage at the focusing hydrophone to the peak pressure of the shock waves at the distance 10 mm from the bubble center is

$$\frac{p_0(10\text{mm})}{u_{\max}} \approx 9.5 \frac{\text{MPa}}{\text{V}}. \tag{12}$$

This is the sensitivity for the focusing hydrophone of 100-mm aperture and 100-mm focal length. The sensitivity of the two 200-mm focal length transducers were determined to be 26 and 17 MPa/V. The larger calibration values for the 200-mm transducers are consistent with their reduced solid angle. These calibration values relate the peak in the measured PCD signals to the peak radiated acoustic pressure 10 mm from the bubble. The shape of the measured PCD signals is related to the impulse response of the PCD transducer and is not an accurate representation of the pressure waveform emitted by the bubbles. Recall, that the demodulation process reduced the signal amplitude by a factor of 2.5 and so the calibration values have to be multiplied by 2.5 when applied to demodulated signals.

F. High-speed camera

High-speed camera images of the focal region were taken with a Kodak EktaPro 4540 (San Diego, CA). The APL-UW lithotripter has a water tank made of optically clear acrylic. The focal region was backlit with either a 400- or a 1000-W light bulb which meant that bubbles appeared as dark regions (shadows) on the image. The camera had a maximum frame rate of 40 500 frames per second and stored up to 5120 full frames in memory. The size of each frame at the maximum framing rate was 64×64 pixels. In these experiments, the focal depth was 3 cm and the image area was 9 by 9 mm. The camera was triggered with the photodiode and operated simultaneously with the dual PCD system, see Fig. 5. The digital images obtained by the camera were stored on videotape and analyzed with NIHImage (National Institutes of Health, Bethesda, MD).

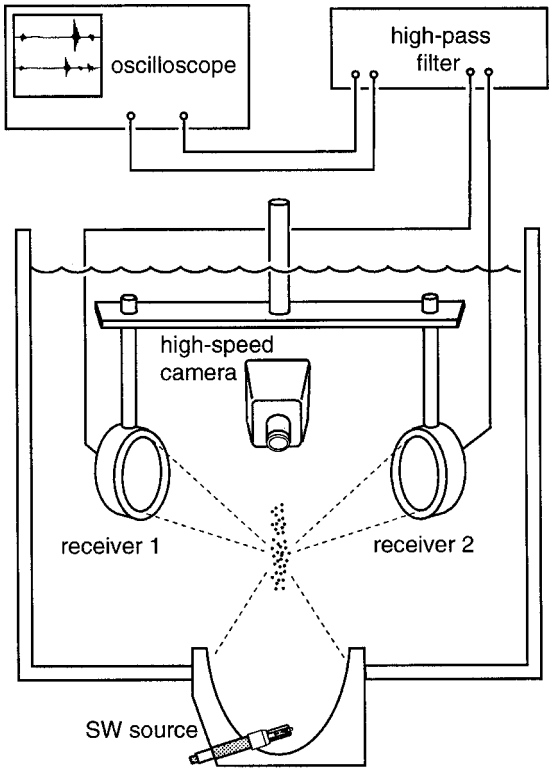

FIG. 5. Setup for high-speed photography and dual PCD.

II. RESULTS

A. Cavitation field of an electrohydraulic lithotripter

We first report on *in vitro* measurements of the cavitation field performed in both the APL-UW lithotripter and the clinical Dornier HM3 lithotripter. Figure 6 shows the characteristic time t_C and collapse pressure p_C of the cavitation at $F2$ for charging voltages between 12 and 24 kV. Twenty shock waves were fired at each voltage and each detected focal event is marked with a ''+.'' The solid line connects the mean values from the focal events. The results from the two lithotripters were similar with an almost monotonic increase in both the radiated pressure at collapse p_C and the characteristic time t_C with applied voltage. The results are in agreement with measurement by others (Coleman *et al.*, 1992; Zhong *et al.*, 1997). We note that the scatter in the measurement of the characteristic time was 20%, whereas the scatter in the peak pressure value was 100%. One reason for the large variation in p_C is that measurements of p_C are highly sensitive to the location of the bubble in the focal region of the dual PCD system, whereas t_C is not. In comparing the two lithotripters we observed that the characteristic times were comparable; however, p_C in the APL-UW lithotripter was about twice that measured in the HM3. One

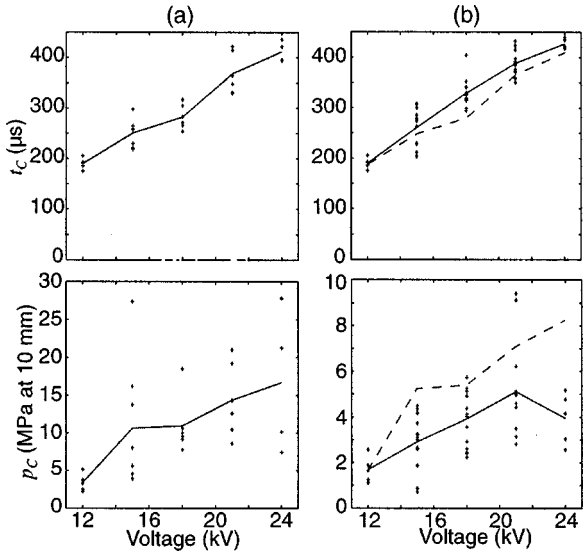

FIG. 6. Measured characteristic time t_C and the radiated collapse pressure p_C as a function of voltage for (a) the APL-UW lithotripter and (b) HM3 lithotripter. The crosses (+) represent individual measurements and the solid line is the mean value. The dashed lines in (b) are mean values for APL-UW lithotripter.

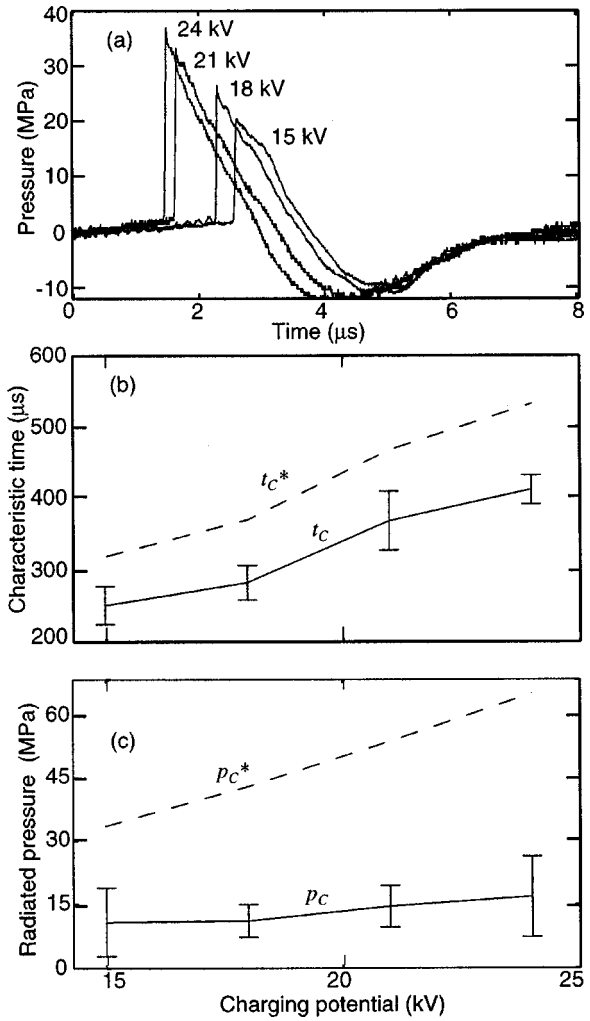

FIG. 7. Comparison between measured and calculated cavitation dynamics (a) measured waveforms used as inputs to the Gilmore–Akulichev model, (b) calculated characteristic time t_C^* (dashed line) and measured t_C (solid line), (c) calculated radiated pressure p_C^* (dashed line) and measured radiated pressure p_C (solid line).

notable difference between the two lithotripters was that the water in the APL-UW lithotripter was at 20 °C and that in the HM3 was at 37 °C. We speculate that the warmer water in the HM3 may have increased diffusion of gas into the bubble and led to a softening of the collapse and reduced radiated pressure.

Figure 7(a) shows pressure waveforms measured at 15, 18, 21, and 24 kV in the APL-UW lithotripter. Plots of the calculated characteristic time t_C^* and calculated collapse pressure p_C^* based on these waveforms are compared to measured values. There is reasonable agreement between the measured and calculated characteristic times. Recall that the negative tail of the pressure waveform was elongated to correct a measurement problem with the hydrophone. The elongation factor was based on the measurements by Wurster *et al.* (1994) and was not used as a free variable to ensure a fit between t_C and t_C^*. Reducing the elongation factor would have brought the calculated values closer to the measured values. Without the correction the calculated characteristic time t_C^* was about one-half of the measured characteristic time t_C. The 20% variation in the measured t_C was reproduced in the calculations by varying the amplitude of the acoustic waveform by 10% (which is the typical variation in the measurements of the peak negative pressure of the shock waves). The comparison between p_C and p_C^* shows that measured and calculated values have the same trends but the calculated values were about four times larger than the measurements. The qualitative correlation between characteristic time, collapse pressure, and discharge voltage has been observed before in both calculations (Church, 1989) and measurements (Coleman *et al.*, 1992). Although correcting the negative phase of the pressure waveforms made it possible to obtain quantitative agreement for the characteristic time; it was not possible to obtain quantitative agreement with the collapse pressure. We have already commented that our model for the radiated pressure neglects nonlinear distortion and that we expect the calculated values to overestimate the pressure. In addition, the model assumes a spherical collapse; in the case of an aspherical collapse one would also anticipate the model to overestimate the radiated pressure. Other losses, such as thermal damping, are also neglected (Church, 1989).

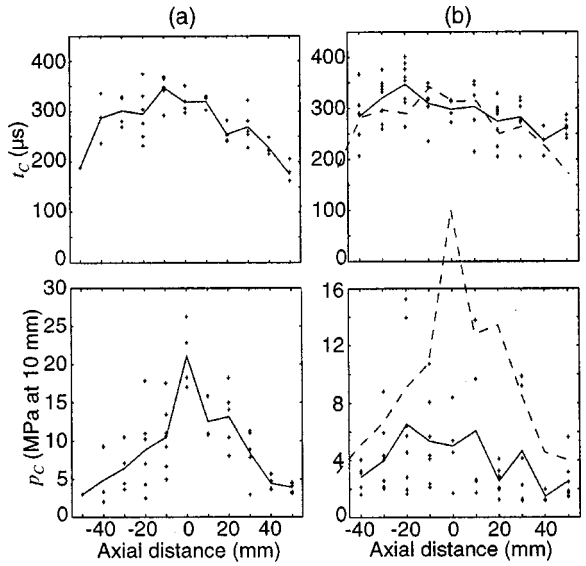

FIG. 8. Axial cavitation field (a) APL-UW lithotripter, (b) HM3 lithotripter (dashed lines are mean values for APL-UW lithotripter). The geometrical focus ($F2$) is at zero and negative distances are toward the source; the spark was fired at 18 kV.

Figure 8 shows the variation of the characteristic time and radiated pressure along the axis of each lithotripter for a fixed charging voltage of 18 kV. The two lithotripters have similar characteristic times but again the radiated pressure in the HM3 is approximately one-half of the APL-UW machine. Data were compared using Student's *t*-test. For the HM3, the maximum t_C occurred at $z=-20$ mm ($p<0.1$); there was no statistically significant peak in p_C. In the APL-UW lithotripter the peak in the characteristic time could not be distinguished between $z=-10$ and $z=0$ mm ($p<0.1$). There was a peak in p_C at $z=0$ mm ($p<0.001$). These results are in agreement with single PCD measurements that showed that the characteristic time peaked about 10 to 20 mm in front of $F2$ (Coleman *et al.*, 1992). It is also consistent with the location of the peak negative pressure in

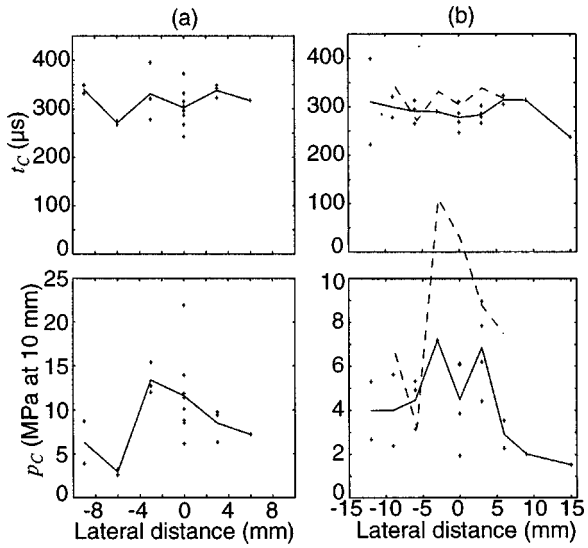

FIG. 9. Lateral scan (at $F2$ and 18 kV) of the cavitation field (a) APL-UW lithotripter, (b) HM3 lithotripter (dashed lines are mean values for APL-UW lithotripter).

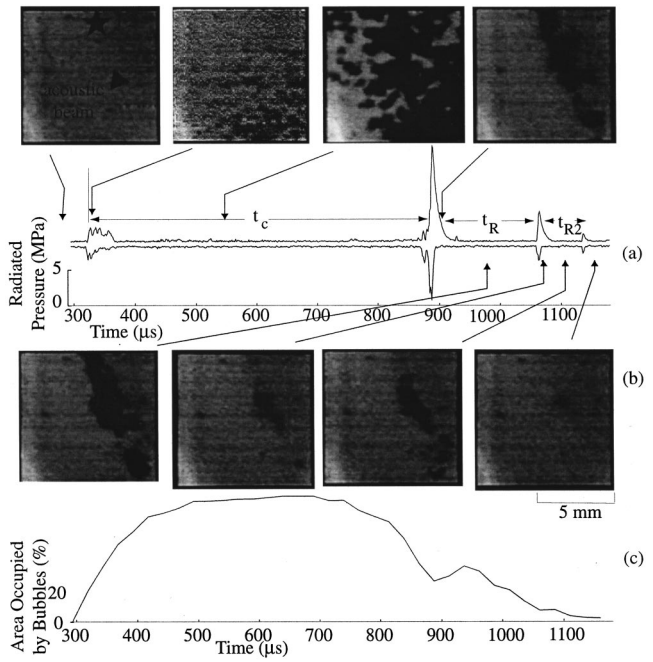

FIG. 10. Bubble rebound as captured by (a) dual PCD, (b) sequence of high-speed camera images and, (c) area occupied by the bubble cloud. The dual PCD traces show spikes representing inertial collapses at 880, 1060, and 1140 μs. These times correspond to a minimum in the size of the bubble cloud.

an electrohydraulic lithotripter as determined by both measurements (Coleman *et al.*, 1989; Cleveland *et al.*, 2000) and numerical simulations (Coleman *et al.*, 1991; Christopher, 1994; Averklou and Cleveland, 1999). The 6-dB length of p_C is approximately 50 mm and it corresponds to (1) the region where the negative pressure in the lithotripter is in excess of -5 MPa (Cleveland *et al.*, 2000), (2) the length of the lithotripsy-induced bubble cloud as determined by high-speed video images (Huber *et al.*, 1994), and (3) the axial size of pitting created in aluminum foil (Bailey *et al.*, 1999).

Figure 9 shows measurements for a transverse scan (at the geometrical focus) of t_C and p_C for a discharge voltage of 18 kV for both lithotripters. Two notable features of the data are (1) that the characteristic time t_C is almost uniform across the beam of the lithotripter and (2) that very few cavitation events were detected more than 5 mm off-axis—despite the fact that the peak negative pressure in the lithotripter exceeds -5 MPa in excess of 10 mm off-axis. Recall that the spatial resolution of the dual PCD is 5 mm and the region of collapse may be even narrower than indicated by Fig. 9. Indeed, high-speed photography presented below shows that the collapse of bubbles occurs almost as a line along the acoustic axis. It appears that during their collapse bubbles are drawn toward the acoustic axis of the lithotripter.

B. High-speed photography and bubble rebound

The apparent rebound signal, seen in Figs. 3 and 4, was investigated using dual PCD and high-speed photography simultaneously. Figure 10 shows (a) dual PCD traces and (b) high-speed video images of the cavitation from a single shot at 18 kV in the APL-UW lithotripter. At 310 μs the shock wave impinged upon bubbles at $F2$ and the first acoustic burst was emitted. The bubbles then grew to form a broad cloud and then collapsed in a line at 900 μs ($t_C = 600\,\mu$s), emitting a second burst measured by the dual PCD. The cloud then rebounded and generated a rebound signal at 1060 μs recorded by the dual PCD. A second rebound was detected at 1140 μs. The correlation between the dual PCD system and the high-speed video images is excellent. It can be seen from the images that although bubbles are generated over a region approximately 8 mm in diameter, the bubbles appear to collapse collectively, as a cylindrical cluster, to a line along the acoustic axis rather than spherically to their center of radius. This is in accordance with other high-speed video images (Zhong *et al.*, 1999) and explains why very few cavitation events were recorded by the dual PCD off-axis (see Fig. 9).

In Fig. 10(c) the size of the bubble cloud is plotted as a function of time. The size of the bubble cloud at each instant was based on the light intensity of each camera frame. The average light intensity $I(t)$ was calculated by averaging over all the pixels [0 (white) to 255 (black)]. A background intensity I_b was obtained from a frame recorded halfway between spark discharge and the arrival of the acoustic wave in the focal area. The corrected intensity $I_c(t) = I(t) - I_b$ was calculated in order to compensate for naturally occurring shadows that varied between tests but were unrelated to the cavitation bubbles. The plot of intensity (bubble cloud size) with time confirms that the bubbles undergo a main growth and collapse followed by rebounds. There is excellent agreement between the minima in the bubble cloud size and the presence of acoustic emissions from the dual PCD.

In Fig. 11 the rebound time t_R and rebound collapse pressure p_R are shown as a function of discharge voltage. These values were obtained from the same data that was used to generate Fig. 6. Rebound events are marked by a ''○'' and the solid line is the average rebound time. The characteristic times t_C associated with the bubbles that had rebounds are marked by ''+'' and the dashed line is the aver-

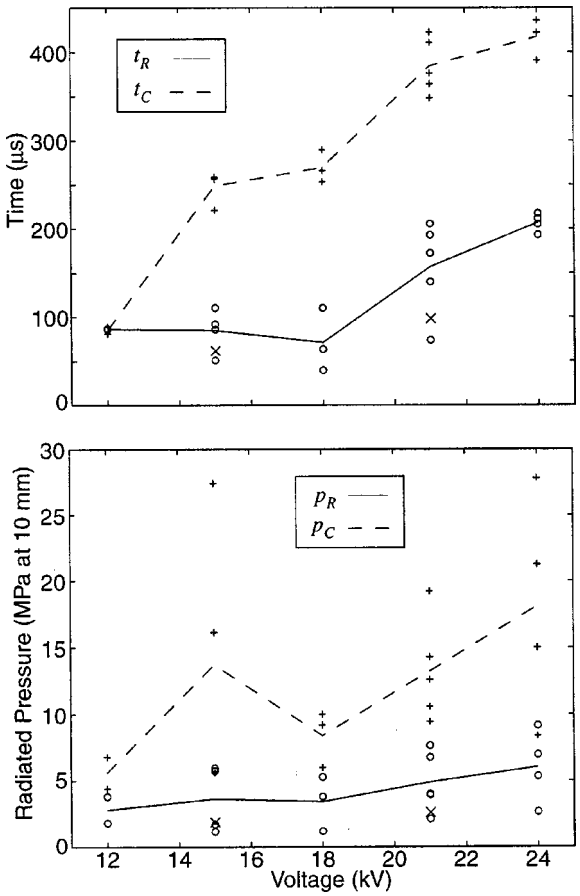

FIG. 11. Bubble duration and collapse pressure for the rebound signal and the main collapse as a function of voltage in the APL-UW lithotripter. Individual rebound events are marked with an ''○'' and the solid line is the mean. Corresponding main collapse events are denoted with a ''+'' and dashed line is the mean. Second rebounds were detected at 15 and 21 kV and are marked by an ''×.''

age value. Only two shots, one at 15 kV and one at 21 kV, produced cavitation that was determined to have two rebounds; these events are marked by ''×.''

In general, the measured rebound times were shorter then the characteristic time $t_R < t_C$ and radiated pressure at rebound was less $p_R < p_C$. Calculations [see, for example, Fig. 1(c)] are in agreement with these trends. The monotonic increase in t_R and p_R with discharge voltage was also in agreement with calculations and is consistent with the fact that at higher voltages the bubbles are driven harder. However, the agreement is qualitative; the measured time t_R was about five times longer than t_R^* and the measured radiated pressure p_R about ten times larger than p_R^*. We note that for the main collapse the measured p_C was smaller than p_C^*. The two second rebound events that were detected had a shorter rebound time and smaller collapse pressure than either the main burst or the rebound, also in qualitative agreement with the model.

Because the main collapse was that of a bubble cloud or cluster it is not surprising that the rebound no longer behaves in accordance with a theory that assumes a single spherical bubble for the entire dynamics. We can model the rebound with the Rayleigh model for a spherical void collapsing in a fluid (see, e.g., Church, 1989). We approximate the collapse time of the void as $t_R/2$. The corresponding maximum bubble radius using Rayleigh's expression is $R_{\max} = (t_R/2)\sqrt{P_0/\rho}/0.915$, where P_0 and ρ are the ambient pressure and density of the liquid. For water, $R_{\max} \approx 5.5 \cdot 10^{-3} t_R$, where $R_{\max}$ is measured in millimeters and t_R in microseconds. The rebound time in Fig. 11 was $t_R = 175\,\mu$s, from which we obtain a maximum bubble size $R_{\max} = 0.5$ mm. This corresponds well to the size of the bubble observed with high-speed photography. It appears that after the main collapse the cavitation field acts as an effective single bubble system; but because of agglomeration of bubbles during the main growth and collapse phase the single rebound bubble is larger than what would be predicted using single-bubble theory for the entire cavitation life cycle.

III. DISCUSSION

The dual passive cavitation detection (dual PCD) system has been developed for the localized detection of cavitation events in the field of a shock wave lithotripter. Two confocal receivers (PCD transducers) were used to detect acoustic emissions from cavitation bubbles. Signal processing techniques were used to resolve coincident signals that originated from a volume approximately 5 mm in diameter. The spatial localization is a significant improvement over a single transducer PCD which is sensitive to signals from a relatively long volume. It was necessary to use both the arrival time and the amplitude of received signals to localize an event to the volume of interest.

A calibration technique was described that was appropriate for estimating the peak pressure of spherically spreading shock waves emitted by collapsing cavitation bubbles. The calibration technique relied on the fact that the pulse duration of the acoustic wave from the cavitation event was much shorter than the resonant period of the PCD transducer. It was also necessary to estimate the pulse duration near the bubble, which was done from previously reported measurements of cavitation bubbles generated by a laser pulse. The calibration is not valid for bubbles collapsing asymmetrically; also for *in vivo* measurements the effects of tissue attenuation would need to be taken into account.

The dual PCD system was used to measure the cavitation fields of two electrohydraulic lithotripters: a Dornier HM3 and the APL-UW research machine. Measurements were compared to predictions of the Gilmore–Akulichev model for a single spherical bubble (Church, 1989). We corroborated previous observations that the cavitation signature can be characterized by two acoustic emissions, ''bursts''; the first associated with the arrival of the lithotripter shock wave and the second, hundreds of microseconds later, resulting from an inertial growth and collapse cycle. The cavitation was quantified in terms of the characteristic time t_C and the radiated pressure at collapse p_C. The two machines were observed to have similar cavitation fields. The measured characteristic times were in agreement with results from single-bubble theory after a correction to the tensile portion of the pressure waveform was applied (Bailey *et al.*, 1999). The peak pressure radiated at the primary collapse of the bubble p_C was measured to be on order of 10 MPa at 10 mm

from the bubble center. The collapse pressure of the APL-UW machine was between 30% to 100% higher than that of the HM3, an effect which may be attributable to the higher water temperature in the HM3. Shot-to-shot variation in p_C was much larger than the variation in t_C and may be because p_C was more sensitive to either variations in the water conditions or shock wave variability associated with the electrohydraulic spark source. The calculated p_C^* values were three to four times larger than the measurements. We suspect that this is because the model is idealized and that effects such as thermal damping of the bubble, asymmetry in bubble shape, and finite-amplitude distortion of the radiated pressure wave have been neglected in the model. The measured values of p_C and t_C increased monotonically with increasing discharge voltage as observed by others (Coleman *et al.*, 1992) and in accordance with calculations.

The dual PCD was used to obtain a spatial map of the cavitation field in both lithotripters. An axial scan of the cavitation field showed that inertial cavitation was detected in the range where the peak negative pressure exceeded -5 MPa. The longest characteristic time and largest radiated pressure occurred approximately 10 to 20 mm in front of the focus which correlated with the location of the maximum peak negative pressure in the lithotripter. These results are consistent with reports that the inertial behavior of lithotripsy-induced cavitation is controlled primarily by the negative pressure of the lithotripsy pulse (Church, 1989; Ding and Gracewski, 1994).

In contrast, a transverse scan at the focus indicated that although t_C was nearly uniform out to 20 mm, p_C dramatically dropped for distances more than 5 mm off-axis. In addition, very few events occurred more than 5 mm off-axis; which was also the size of the sensitive region of the dual PCD. The peak negative pressure in the lithotripters exceeds -5 MPa to a distance of at least 12 mm and so one would expect that cavitation field to be at least 25 mm in diameter. High-speed photography indicated that the lithotripter pulse created a cloud of bubbles that collapsed collectively along the axis rather than individually to their own center. Therefore the response of cavitation bubbles off-axis was not simply related to the negative pressure of the shock wave. It appeared that cloud dynamics strongly affected the off-axis bubble dynamics and high-speed video images indicated that the bubbles were attracted to the axis.

The dual PCD system also provided the ability to detect bubble rebounds that occurred after the main collapse. A single PCD would not provide enough specificity to distinguish between a rebound and a second bubble collapsing with a long t_C. High-speed photography confirmed that the coincident events detected by the dual PCD after the primary collapse did indeed coincide with rebounds of the bubble cloud. Comparison with calculations provided only qualitative agreement. However, the rebound times and maximum bubble radius of the rebound observed on the high-speed photography were in agreement with Rayleigh collapse theory.

In conclusion, we have demonstrated an effective new technique for localized passive cavitation detection in the case of shock wave lithotripsy. An algorithm was developed to ensure that detected events originated from a volume about 5 mm in diameter. A novel calibration technique allowed the peak pressure radiated by the bubble to be estimated. It was seen that the measured characteristic time of the bubbles t_C was close to that predicted by single-bubble theory, whereas the pressure radiated at collapse p_C and subsequent bubble dynamics were not. It appeared that once the bubbles started to collapse, cloud dynamics affected the system and single-bubble theory was no longer appropriate. It is planned to use the dual PCD system *in vivo*. Preliminary results indicate that the coincidence algorithm can be used to localize cavitation *in vivo*, as the variations in speed of sound through tissue are small enough that arrival times across different paths should vary by less than 1.5 μs (a localization error of less than 1 mm). What has not yet been accounted for is the effect of tissue absorption on the calibration technique.

ACKNOWLEDGMENTS

The authors would like to thank Dr. Vera Khokhlova and Dr. Michalakis Averkiou for assistance with coding the solution to the Gilmore equation and Dr. James McAteer for valuable discussions. This work was supported by a grant from NIH, No. P01 DK43881 including a supplementary Fogarty International Research Collaboration Award (FIRCA), Grant No. NIH R03 TW00492, and by a Civilian Research and Development Fund (CRDF) Young Investigator Award No. RB2-131.

[1]Although the area under the waveform curve must be zero for a spherical wave (Landau and Lifshitz, 1987) it is likely that the pressure waveform measured by Vogel and Lauterborn had a long weak negative tail which can be neglected as has been done in Eq. (7). For the purpose of the calibration it is only the energy contained in a time scale much less than 1 μs that is important and so Eq. (7) is appropriate.

[2]For the case of a waveform with a negative tail the integral could be modified to the area of the leading positive portion only. Weak shock theory predicts that the area of the positive section alone will also remain constant.

Akulichev, V. A. (**1971**). in *High-Intensity Ultrasonic Fields*, edited by L. D. Rozenberg (Plenum, New York), pp. 239–259.

Averkiou, M. A., and Cleveland, R. O. (**1999**). ''Modeling of an electrohydraulic lithotripter with the *KZK* equation,'' J. Acoust. Soc. Am. **106**, 102–112.

Bailey, M. R., Blackstock, D. T., Cleveland, R. O., and Crum, L. A. (**1999**). ''Comparison of electrohydraulic lithotripters with rigid and pressure-release ellipsoidal reflectors: II. Cavitation fields,'' J. Acoust. Soc. Am. **106**, 1149–1160.

Blackstock, D. T., Hamilton, M. F., and Pierce, A. D. (**1998**). ''Progressive waves in lossless and lossy fluids,'' in *Nonlinear Acoustics*, edited by M. F. Hamilton and D. T. Blackstock (Academic, New York).

Cathignol, D., Sapozhnikov, O. A., and Zhang, J. (**1997**). ''Lamb waves in piezoelectric focused radiator as a reason for discrepancy between O'Neil's formula and experiment,'' J. Acoust. Soc. Am. **101**, 1286–1297.

Chaussy, C., Brendel, W., and Schmiedt, E. (**1980**). ''Extracorporeally induced destruction of kidney stones by shock waves,'' Lancet **2**, 1265–1268.

Chaussy, C., ed. (**1982**). *Extracorporeal Shock Wave Lithotripsy: New Aspects in the Treatment of Kidney Stone Disease* (Karger, Basel).

Choi, M. J., Coleman, A. J., and Saunders, J. E. (**1993**). ''The influence of fluid properties and pulse amplitude on bubble dynamics in the field of a shock wave lithotripter,'' Phys. Med. Biol. **38**, 1561–1573.

Christopher, P. T. (**1994**). ''Modeling the Dornier HM3 lithotripter,'' J. Acoust. Soc. Am. **96**, 3088–3095.

Church, C. C. (**1989**). ''A theoretical study of cavitation generated by an extracorporeal shock wave lithotripter,'' J. Acoust. Soc. Am. **86**, 215–227.
Cleveland, R. O., Bailey, M. R., Hartenbaum, B., Fineberg, N., Lokhandwalla, M., McAteer J. A., and Sturtevant, B. (**2000**). ''Design and characterisation of a research electrohydraulic lithotripter patterned after the Dornier HM3,'' Rev. Sci. Instrum. (accepted).
Coleman, A. J., Saunders, J. E., Crum, L. A., and Dyson, M. (**1987**). ''Acoustic cavitation generated by an extracorporeal shockwave lithotripter,'' Ultrasound Med. Biol. **13**, 69–76.
Coleman, A. J., and Saunders, J. E. (**1989**). ''A survey of the acoustic output of commercial extracorporeal shock wave lithotripters,'' Ultrasound Med. Biol. **15**, 213–227.
Coleman, A. J., Choi, M. J., and Saunders, J. E. (**1991**). ''Theoretical predictions of the acoustic pressure generated by a shock wave lithotripter,'' Ultrasound Med. Biol. **17**, 245–255.
Coleman, A. J., Choi, M. J., Saunders, J. E., and Leighton, T. G. (**1992**). ''Acoustic emission and sonoluminescence due to cavitation at the beam focus of an electrohydraulic shock wave lithotripter,'' Ultrasound Med. Biol. **18**, 267–281.
Coleman, A. J., Choi, M. J., and Saunders, J. E. (**1996**). ''Detection of acoustic emission from cavitation in tissue during clinical extracorporeal lithotripsy,'' Ultrasound Med. Biol. **22**, 1079–1087.
Crum, L. A. (**1988**). ''Cavitation microjets as a contributory mechanism for renal calculi disintegration in ESWL,'' J. Urol. (Baltimore) **40**, 1587–1590.
Dalecki, D., Raeman, C. H., Child, S. Z., and Carstensen, E. L. (**1996**). ''A test for cavitation as a mechanism for intestinal hemorrhage in mice exposed to a piezoelectric lithotripter,'' Ultrasound Med. Biol. **22**, 493–496.
Delacretaz, G., Rink, K., Pittomvils, G., Lafaut, J. P., Vandeursen, H., and Boving, R. (**1995**). ''Importance of the implosion of ESWL-induced cavitation bubbles,'' Ultrasound Med. Biol. **21**, 97–103.
Delius, M., Denk, R., Berding, C., Liebich, H., Jordan, M., and Brendel, W. (**1990**). ''Biological effect of shock waves: Cavitation by shock waves in piglet liver,'' Ultrasound Med. Biol. **16**, 467–472.
Ding, Z., and Gracewski, S. M. (**1994**). ''Response of constrained and unconstrained bubbles to lithotripter shock wave pulses,'' J. Acoust. Soc. Am. **96**, 3636–3644.
Eller, A., and Flynn, H. G., (**1965**). ''Rectified diffusion during nonlinear pulsations of cavitation bubbles,'' J. Acoust. Soc. Am. **37**, 493–501.
Evan, A. P., and McAteer, J. A. (**1996**). ''*Q*-Effects of shock wave lithotripsy, in *Kidney Stones: Medical and Surgical Management*, edited F. Coe, C. Pak, and G. M. Preminger (Raven, New York), pp. 549–570.
Gilmore, F. R. (**1952**). *The Growth or Collapse of a Spherical Bubble in a Viscous Compressible Liquid* (California Institute of Technology, Pasadena, CA), Rep. No. 26-4, pp. 1–40.
Holmes, S. A. V., and Whitfield, H. N. (**1991**). ''The current status of lithotripsy,'' Br. J. Urol. **68**, 337–344.
Howard, D. D., and Sturtevant, B. (**1997**). ''*In vitro* study of the mechanical effects of shockwave lithotripsy,'' Ultrasound Med. Biol. **23**, 1107–1122.
Huber, P., Debus, J., Peschke, P., Hahn, E. W., and Lorenz, W. J. (**1994**). ''*In vivo* detection of ultrasonically induced cavitation by a fibre-optic technique,'' Ultrasound Med. Biol. **20**, 811–825.
Huber, P., Debus, J., Jöchle, K., Simiantonakis, I., Jenne, J., Rastert, R., Spoo, J., Lorenz, W. J., and Wannenmacher, M. (**1999**). ''Control of cavitation activity by different shockwave pulsing regimes,'' Phys. Med. Biol. **44**, 1427–1437.
Jochle, K., Debus, J., Lorenz, W. J., and Huber, P. (**1996**). ''A new method of quantitative cavitation assessment in the field of a lithotripter,'' Ultrasound Med. Biol. **22**, 329–338.
Kaude, J. V., Williams, C. M., Millner, M. R., Scott, K. N., and Finlayson, B. (**1985**). ''Renal morphology and function immediately after extracorporeal shock-wave lithotripsy,'' Am. J. Roentgenol. **145**, 305–313.
Landau, I. D., and Lifshitz, E. M. (**1987**). *Fluid Mechanics*, 2nd ed. (Pergamon, New York).
Lifshitz, D. A., Williams, Jr., J. C., Sturtevant, B., Conners, B. A., Evan, A. P., and McAteer, J. A. (**1997**). ''Quantization of shock wave cavitation damage *in vitro*,'' Ultrasound Med. Biol. **23**, 461–471.
Lingeman, J. E. (**1996**). ''Extracorporeal shock wave lithotripsy devices: Are we making progress,'' in *New Developments in the Management of Urolithiasis*, edited by J. E. Lingeman and G. M. Preminger (Igaku-Shoin, New York).
O'Neil, H. T. (**1949**). ''Theory of focusing radiators,'' J. Acoust. Soc. Am. **21**, 516–526.
Press, W. H., Teukolsky, S. A., Vetterling, W. T., and Flannery, B. P. (**1992**). *Numerical Recipes in Fortran*, 2nd ed. (Cambridge University Press, Cambridge).
Pye, S. D., and Dineley, J. A. (**1999**). ''Characterization of cavitational activity in lithotripsy fields using a robust electromagnetic probe,'' Ultrasound Med. Biol. **3**, 451–471.
Rudenko, O. V., and Soluyan, S. I. (**1977**). *Theoretical Foundations of Nonlinear Acoustics* (Plenum, New York).
Sass, W., Braunlich, M., Dreyer, H.-P., Matura, E., Folberth, W., Priesmeyer, H.-G., and Seifert, J. (**1991**). ''The mechanisms of stone disintegration by shock waves,'' Ultrasound Med. Biol. **17**, 239–243.
Vogel, A., and Lauterborn, W. (**1988**). ''Acoustic transient generation by laser-produced cavitation bubbles near solid boundaries,'' J. Acoust. Soc. Am. **84**, 719–731.
Wurster, C., Staudenraus, J., and Eisenmenger, W. (**1994**). ''The fibre optic probe hydrophone,'' Nature (London) **2**, 941–944.
Zhong, P., Cioanta, I., Cocks, F. H., and Preminger, G. M. (**1997**). ''Inertial cavitation and associated acoustic emission produced during electrohydraulic shock wave lithotripsy.'' J. Acoust. Soc. Am. **101**, 2940–2950.
Zhong, P., Cioanta, I., Zhu, S., Cocks, F. H., and Preminger, G. M. (**1998**). ''Effects of tissue constraint on shock-wave induced bubble expansion *in vivo*,'' J. Acoust. Soc. Am. **104**, 3126–3129.
Zhong, P., Lin, H., Xi, X., Zhu, S., and Bhogte, E. S. (**1999**). ''Shock wave-inertial microbubble interaction: Methodology, physical characterization and bioeffect study,'' J. Acoust. Soc. Am. **105**, 1997–2009.